

Towards a mechanical MPI scanner based on atomic magnetometry

Simone Colombo^{a,*} · Victor Lebedev^a · Alexey Tonyushkin^b · Zoran D. Grujić^a · Vladimir Dolgovskiy^a · Antoine Weis^a

^aPhysics Department, University of Fribourg, Chemin du Musée 3, 1700 Fribourg, Switzerland

^bPhysics Department, University of Massachusetts Boston, Boston, MA 02125 USA

*Corresponding author, email: simone.colombo@unifr.ch

Abstract

We report on our progress in the development of an atomic magnetometer (AM) based low-frequency Magnetic Particle Imaging (MPI) scanner, expected to be free from Specific Absorption Rate (SAR) and Peripheral Nerve Stimulation (PNS) constraints. We address major challenges in coil and sensor design due to specific AM properties. Compared to our previous work we have changed the AM's mode of operation towards its implementation for detecting the weak magnetic field produced by magnetic nanoparticles (MNP) in the presence of nearby-located strong drive/selection fields. We demonstrate that a pump-probe AM scheme in a buffer gas filled alkali vapour cell can tolerate mT/m gradients while maintaining a sensitivity in the one-digit pT/ $\sqrt{\text{Hz}}$ range over a bandwidth from DC to several kHz. We give a detailed description of the drive/selection coils' geometry and their hardware implementations that provides field-free-line (FFL) operation, compatible with a best performance AM operation. We estimate the achievable field of view and spatial resolution of the scanner as well as its sensitivity, assuming mechanical scanning of a Resovist sample through the field-free point/line.

I. Introduction

Since its invention in 2005 [1] Magnetic Particle Imaging (MPI) has developed into a mature technology with a number of variants and designs [2, 3, 4]. All MPI implementations are based on the detection of the MNP response to an oscillating drive field produced by transmit coils. The detection by resonant (or non-resonant [5]) receive coils relies on Faraday's induction law, implying a voltage signal proportional to the drive frequency. The detection efficiency of the oscillating MNP magnetization $M(t)$ used to encode the sample's spatial density distribution is thus favoured for high frequency excitation. However, concerns have been raised about the specific absorption rates, which depend on the drive field's amplitude and frequency in a similar manner as the MNP response proper [6]. This feature limits the frequency and amplitude of the drive field, thus affecting both the sensitivity and spatial resolution of the method.

Replacing the pick-up coil with a sensitive magnetic field sensor with a flat frequency response (down to DC) may circumvent the above mentioned limitations. An analysis of the performance of state-of-the-art MPI systems shows that this alternative detection method calls for a magnetometer with magnetic sensitivity in the lower pT range, preferably reaching 100 fT, and having a flat

frequency response up to several 10 kHz.

Following our successful demonstration that magnetic particle spectra (MPS) can be recorded with a state-of-the-art atomic magnetometer (AM) [7, 8], we are in the process of developing an AM-based MPI system aiming at a competitive sensitivity and resolution, while deploying drive frequencies in the lower (or sub-) kHz frequency range.

Atomic magnetometers, also known as optical magnetometers or optically pumped atomic magnetometers, measure the magnetic field by the optical readout of the Larmor precession frequency

$$f_L = \gamma |\vec{B}| = \gamma B \quad \left(\gamma = \frac{\mu_B}{h(I+1/2)} \approx 3.5 \text{ Hz/nT} \right), \quad (1)$$

of spin-polarized paramagnetic atoms in the magnetic flux density $B(t) \propto M(t)$ of interest. In Eq. (1) μ_B is the Bohr magneton, h Planck's constant, and $I=7/2$ the nuclear spin of the ^{133}Cs atoms used in the magnetometer. We note that B represents the average flux density in the intersection volume V of the pump and probe beams (see Fig. 1). An AM sensor is a sealed glass bulb containing a vapour of the sensing atoms, ^{133}Cs in our case. Circularly-polarized resonant laser light (pump beam) produces the required spin polarization. A second beam (probe beam) – derived from the same or another laser – reads out the

spin precession that is impressed by a magnetic resonance process as a power or polarization modulation onto the transmitted probe beam.

The sensitivity of the AM scales with the amount of sensing atoms, i.e., with the volume V , but degrades when the flux density changes over the sensed volume, since inhomogeneous B -fields broaden the magnetic resonance line. The AM deployed in our initial MPS experiments [7, 8] could reach a sensitivity of $200 \text{ fT}/\sqrt{\text{Hz}}$ in a 2 kHz bandwidth under optimal conditions, i.e. in a homogeneous field inside state of art magnetic shielding. However, such AM originally designed for the fT-performance under shielded conditions, stopped working in the ambient field gradients above 0.2 mT/m , a value much smaller than typical fringe field amplitudes in the vicinity of any MPI/MPS coils. Demand for high sensitivity in presence of strong field gradients lead us to the development of self-compensating solenoids for MNP magnetization, reducing the fringe drive field at the sensor position by a factor of 10^4 compared to the field at the sample position (in presence of a 1 T/m gradient at the sample position). In that geometry the magnetometric sensitivity was reduced to a few $\text{pT}/\sqrt{\text{Hz}}$, and the drive coil design did not allow us to convert the system into a simple MPI scanner.

Here we describe our recent improved design of the experimental set-up, in particular the sensor and coil, in view of developing an operational 2D MPI scanner and its future upgrade to a volumetric scanner.

II. Optical magnetometer

The operation of our magnetometer is sketched in Fig. 1. The circularly-polarized pump laser beam ($\lambda \sim 894 \text{ nm}$) is resonant with the $4 \rightarrow 3$ hyperfine component of the $6S_{1/2} \rightarrow 6P_{1/2}$ (D_1) atomic transition spin-polarizes the cesium atoms by optical pumping, see Chapter 4 in [9]. The probe laser beam is linearly-polarized and its polarization is analyzed by a balanced polarimeter. The system is operated in a magnetically unshielded environment, in which the local laboratory field is compensated and an offset field B_0 of $\approx 27 \mu\text{T}$ (corresponding to a Larmor frequency of $\approx 100 \text{ kHz}$) along x is applied to the atoms.

A weak radio frequency magnetic field (rf-field) oscillating along the z direction is used to resonantly drive the atomic spin polarization produced by the pump beam on a cone around the x axis, leading to an oscillating component polarization along the probe beam direction. This oscillating component induces a corresponding oscillation of the direction of the probe beam's linear polarization that is detected by the balanced polarimeter. A phase detector (marked Φ) and a voltage controlled oscillator (VCO) drive the rf-coil. When exposed to a time-independent field $\vec{B}_0 \parallel \hat{x}$, the oscillation frequency of this phase-locked loop is proportional to B_0 , following Eq. (1). Any component $\delta B_x(t)$ of a time-dependent field along

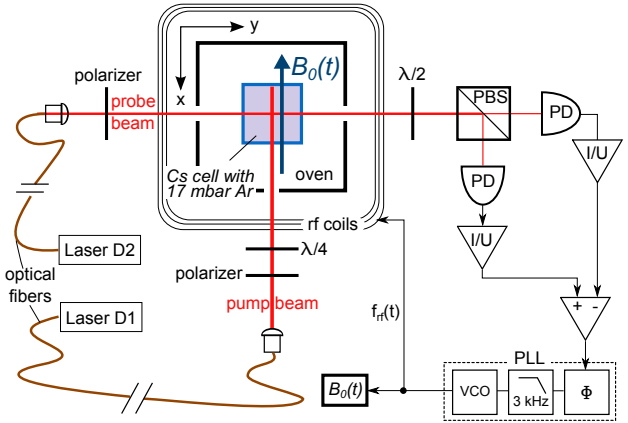


Figure 1: Sketch of the magnetometry part of the apparatus with polarizing beam splitter (PBS), photodiode (PD), current-to-voltage converter (I/U), and voltage-controlled oscillator (VCO).

\vec{B}_0 – such as the one produced by the harmonically driven MNP sample – will thus induce a frequency modulation, whose amplitude ($\propto \delta B_x$) can be extracted by a suitable demodulation technique [8].

We stress that only field components $\delta \vec{B}$ parallel to \vec{B}_0 yield a linear response, since they change the Larmor frequency in a linear manner, while transverse components yield only second order corrections.

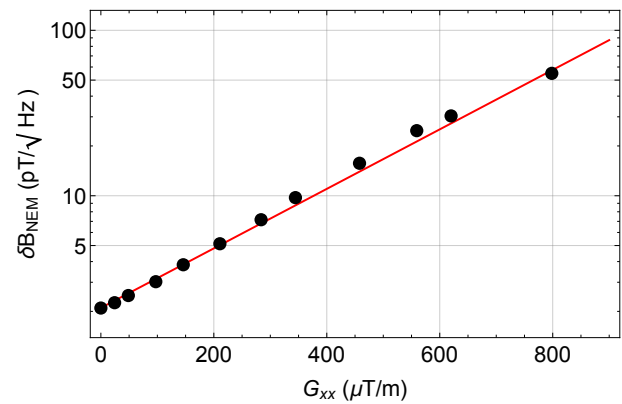


Figure 2: Magnetometer sensitivity (defined as noise-equivalent magnetic flux density, NEM) as a function of field gradient in the sensor volume.

To improve the performance of our AM in the presence of field gradients, the sensing volume must have the smallest possible size, such that magnetic resonance line broadening due to field variations over the volume is minimized. Argon buffer gas at 17 mbar limits the diffusive motion of the spin-polarized Cs atoms to the region illuminated by the pump laser beam. The sensing volume is then further constrained by having the (orthogonally propagating) pump and probe beams intersect in a volume of $\approx 2 \times 2 \times 2 \text{ mm}^3$. Since the magnetometric sensitivity depends on the number of contributing atoms,

the small sensing volume implies the need to increase the atomic density, itself proportional to the saturated vapor pressure. For this reason the cell is installed inside a miniature oven ($\approx 7 \times 7 \times 5 \text{ cm}^3$) heated to an optimized temperature of 55°C .

We have tested the performance of the AM in presence of field gradients. For this we exposed the AM to a quadrupole field with a linear gradient $G_{xx} = dB_x/dx$ along the offset field \vec{B}_0 . The results are shown in Fig. 2.

III. Coil design

Designing the coils for operating an MPI scanner based on atomic magnetometry is a very delicate task. The selection coils should produce a gradient on the order of T/m at the sample position, while the fringe field of that coil at the AM position must be as small and homogeneous as possible in order to achieve an optimal sensitivity. Figure 2 shows that in a gradient G_{xx} of $500 \mu\text{T/m}$ our magnetometer has a sensitivity δB_{NEM} of $\approx 20 \text{ pT}/\sqrt{\text{Hz}}$. When aiming at a gradient of 1 T/m at the MNP sample position, one has thus to insure that the stray gradient 'seen' by the magnetometer is suppressed by a factor of at least 2'000 with respect to that value.

On the other hand one needs to ensure that the detected modulated field component $\delta B_x(t)$ produced by the MNP sample in the sensor is not significantly perturbed by a fringe field component of the modulation field $H^{\text{mod}}(t)$.

We produce the MNP selection and modulation fields by means of elongated coils [10, 11] shown in Fig. 3 (selection coils in light-red and modulation coils in blue). Each of the 300 mm long coils consists of 39 layers of copper tape with a $6.25 \times 0.25 \text{ mm}^2$ cross-section, isolated by a $25 \mu\text{m}$ thick Kapton insulator on one side. The vertical extension of the coil is 40 mm yielding an aspect-ratio larger than 7. The coils have the advantage of being mechanically very stable and sustaining a large current density without significant heating.

The selection coils are placed in an oppositely-poled configuration (quadrupole field) which creates a field free line (FFL) extending along the y -axis. For an aperture $\Delta x = 20 \text{ mm}$ (defined in Fig. 4 and allowing a geometrically accessible $10 \times 40 \text{ mm}^2$ field of view, FOV) the gradient scales with current as

$$\frac{dG_{xx}^{\text{sel}}}{dI} = -\frac{dG_{zz}^{\text{sel}}}{dI} = 0.1 \frac{\text{T}}{\text{m}} \text{A}^{-1}. \quad (2)$$

At the magnetometer, located at $z^{\text{AM}} = -75 \text{ mm}$ below the FFL, the selection coils produce the fringe field pattern shown in Fig.5.a. The graphs *b* and *c* of that figure show the relevant gradients that influence the AM sensitivity. The field patterns produced by the selection coils at both the sample and the AM positions are well approximated by the field from four infinitely long rods carrying the

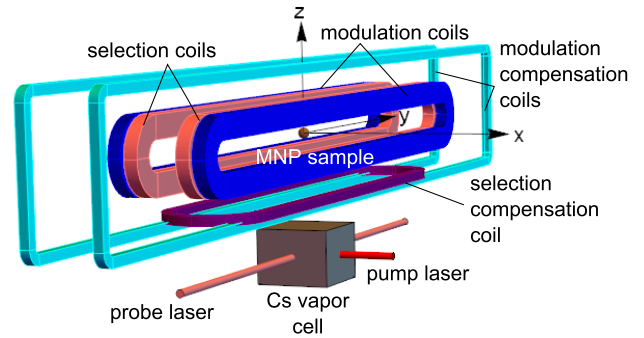


Figure 3: Sketch (to scale) of the coil design for the proposed MPI scanner. Race-tracks represent different current-carrying coils: pink – the selection coils, purple – the selection compensation coil, blue – the modulation coils, and cyan – the modulation compensation coils. The directions of current flow are given in Fig. 4.

same total current and having the same cross-section as the actual coils. The 10 A current needed to produce a gradient of $G_{xx}^{\text{sel}}(z^{\text{sample}})$ of $\approx 1 \text{ T/m}$ at the MNP sample position produces a B_z^{sel} field component of $\approx 260 \mu\text{T}$ and

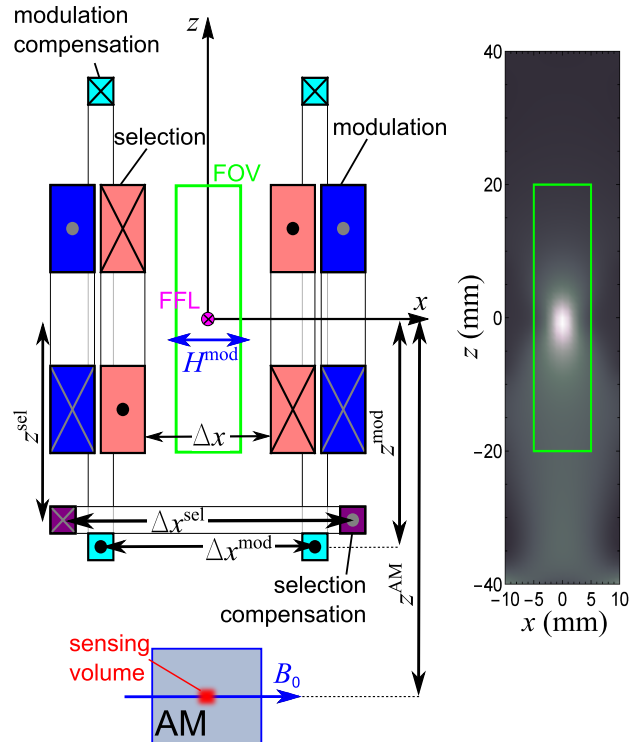


Figure 4: Left: Cross-sectional view (to scale) of the deployed coils. The green rectangle indicates the field of view (FOV) in the $y=0$ plane limited by (not shown) mechanical components. Right: Anticipated point spread function (image produced by a point-like sample) in a gradient $\mu_0 G_{xx} = H_k / \text{mm}$. The green rectangle delimits the FOV.

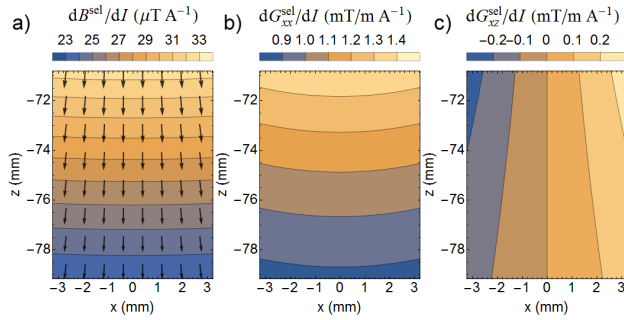


Figure 5: Simulated fringe field from the *selection coils* (a) and its two gradient components G_{xx} (b) and G_{xz} (c) at the AM position, located in the $y=0$ plane, where $B_y = 0$.

a gradient $G_{xx}^{\text{sel}}(z^{\text{AM}})$ of ≈ 11 mT/m at the AM position.

For the above reasons we need compensation coils that suppress the fringe fields from both the selection coil and the modulation coil at the AM position.

III.I. Selection field compensation

In a simulation calculation we have tuned the aspect ratio and the position of the coil (shown in purple in Fig.3) that compensate the selection field's fringe field at the magnetometer position. The tuning criteria are the simultaneous minimization of the gradients G_{xx}^{sel} , G_{xz}^{sel} as well as the B_z^{sel} field component at the sensor position. In order to perform this tuning we have fitted the field component B_z and the gradients G_{xx} and G_{xz} induced by two infinitely long wires with oppositely flowing current to the corresponding fringe field/gradients of the selection coils. The parameters of this fitting procedure are the spacing Δx^{sel} between the wires, the vertical position z^{sel} and the ratio α^{sel} between the *total* selection compensation current and the selection coil current. Reversing the compensation current then yields a field pattern that locally compensates B_z^{sel} , G_{xx}^{sel} and G_{xz}^{sel} leaking from the selection coils. The infinitely long rods used in the modeling transfer to the real world as multiple loops of copper wire wound on a racetrack support having Δx^{sel} as aperture in the x -direction and an extension Δy^{sel} in the y -direction. For an aperture $\Delta x = 20$ mm of the selection coils we obtain the following parameters for the selection compensation coil $\Delta x^{\text{sel}} = 42.5$ mm, $\Delta y^{\text{sel}} = 280$ mm, $z^{\text{sel}} = -39$ mm and $\alpha^{\text{sel}} = 5.6$.

III.II. Modulation field compensation

The modulation coils (shown in blue in Figs. 3,4) produce an oscillating homogeneous field oriented along the x -axis at the MNP sample position. For the geometry shown in Fig. 4 and an aperture Δx of 20 mm, the field's amplitude produced by the modulation coils at the sample position scales with current as $dB_x^{\text{mod}}/dI = 0.76$ mT A $^{-1}$. At the sensor position the modulation coils produce the

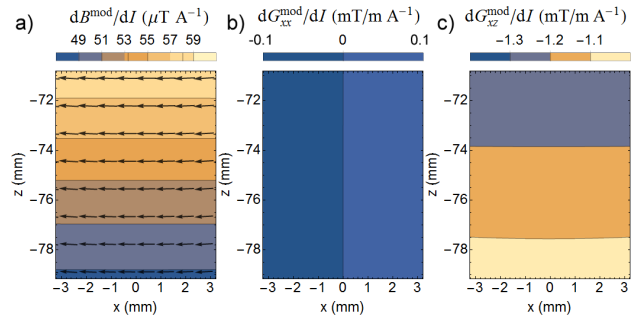


Figure 6: Simulated fringe field amplitude from the *modulation coils* (a) and its two gradient components G_{xx} (b) and G_{xz} (c) at the AM position, located in the $y=0$ plane, where $B_y = 0$.

field amplitude pattern shown in Fig.6.a. The gradients G_{xx}^{mod} and G_{xz}^{mod} leaking from those coils are very small as shown in Fig.6.b-c. As with the selection coils, the pattern produced by the modulation coils in the region of interest is well approximated by one of four infinitely long rods with the same cross-section and carrying the same total current as the coils.

The spacing Δx^{mod} between the two modulation compensation coils and their vertical extension are chosen to minimize simultaneously the gradient components G_{xx}^{mod} and G_{xz}^{mod} as well as the field component B_x^{mod} . The procedure follows the one outlined for the selection coils. We fit the component B_x and the gradients G_{xx} and G_{xz} produced – at the sensor position – by two infinitely long wires to optimize the spacing Δx^{mod} between the wires, the vertical position z^{mod} and the ratio α^{mod} between the *total* modulation compensation current and the modulation coil current. Reversing the compensation current then minimizes the total field/gradients at the AM position. In the apparatus the modelled modulation compensation system is realized as two extended rectangular coils (cyan in Fig.??) with multiple loops. The vertical extension and spacing of the coils are $2|z^{\text{mod}}|$ and Δx^{mod} , respectively. For an aperture Δx of 20 mm we get the optimized parameters $\Delta x^{\text{mod}} = 27$ mm, $z^{\text{mod}} = -45.6$ mm and $\alpha^{\text{mod}} = 4.8$.

III.III. Performance

The coil system described above allows controlling the selection and modulation fields leading to a low field/gradient region at a distance of ≈ 75 mm from the sample at levels that do not significantly degrade the magnetometer's sensitivity.

We have measured the magnetic field's noise spectral density δB_{NEM} of the AM described in Sec. II with and without gradient ($G_{xx}^{\text{sel}} = -G_{zz}^{\text{sel}} = 0.5$ T/m) applied at the MNP location. The respective spectra are shown in Fig.7. While the unperturbed magnetometer reaches sub-pT/ $\sqrt{\text{Hz}}$ sensitivity in the range of 30-300 Hz and below 2 pT/ $\sqrt{\text{Hz}}$ in the 0.3-1 kHz range (blue trace in Fig. 7), the

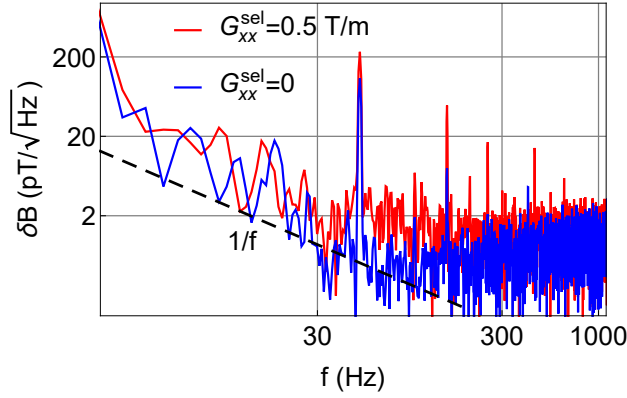


Figure 7: AM sensitivity with and without powered MPI selection coils. G_{xx}^{sel} denotes the gradient at the MNP location for respective plot traces. The dashed line marked '1/f' is meant to guide the eye.

presence of the gradient raises the noise level to a value of ≈ 2 pT/ $\sqrt{\text{Hz}}$ in the 30-1000 Hz (red trace in Fig. 7).

In the low frequency range (<30 Hz) we observe noise decaying like $\delta B \propto 1/f$. This noise is attributed to ambient field and power supply instabilities and not to the magnetometer performance proper. Since our scanner is based on a double modulation technique, as described in Ref. [8], we just need to detect a magnetic signal oscillating in the frequency band around a chosen modulation field frequency. We have thus proven that we can operate the proposed scanner in the frequency range 30-1000 Hz without loss in sensitivity.

IV. Simulation of the signal and point spread function

The general idea of our scanner is closely related to the x -space variant of MPI [3]. The selection field will saturate all particles except those located close to the field free line (FFL). By adding a harmonically oscillating field $\vec{H}^{\text{mod}}(t)$ to the selection field \vec{H}^{sel} , only the unsaturated MNPs will induce a modulation $\delta \vec{B}_{\text{mod}}$ of the flux density at the sensor position. The signal of interest is the amplitude δB_{mod} of that field oscillation, which is proportional to the integral contribution of all particles located along the FFL. When mechanically moving the sample with respect to the FFL, one can thus acquire an image of the MNPs' density distribution. Conversely to standard MPI techniques our scanner works on the direct detection of the MNP response at the drive frequency. Detection of higher harmonics can also be envisioned.

The AM, located at \vec{r}_{AM} , measures variations $\delta B_x(t)$ of the field component B_x induced by the magnetization of the MNP sample. The flux density produced at the sensor location \vec{r}_{AM} by a point-like magnetic moment $\vec{\mu}_s$ located

at \vec{r}_s is given by

$$\delta \vec{B} = \frac{\mu_0}{4\pi} \left[3 \frac{[(\vec{r}_{\text{AM}} - \vec{r}_s) \cdot \vec{\mu}_s] (\vec{r}_{\text{AM}} - \vec{r}_s)}{|\vec{r}_{\text{AM}} - \vec{r}_s|^5} - \frac{\vec{\mu}_s}{|\vec{r}_{\text{AM}} - \vec{r}_s|^3} \right] \quad (3)$$

and the measured component is given by

$$\delta B_x = \delta \vec{B} \cdot \hat{x}. \quad (4)$$

The magnetic moment depends on the local field $\vec{H}(\vec{r}_s)$ and is described – in the approximation of a monodisperse MNP suspension – by the Langevin model function

$$\vec{\mu}_s(\vec{r}_s) = \mu_s \hat{H}(\vec{r}_s) \mathcal{L} \left(\frac{|\vec{H}(\vec{r}_s)|}{H_k} \right), \quad (5)$$

with $\mathcal{L}(x) = \coth(x) - x^{-1}$ and $\hat{H}(\vec{r}_s) \equiv \vec{H}(\vec{r}_s) / |\vec{H}(\vec{r}_s)|$ denotes the direction of the local field. The latter is produced by the coil system (selection coils, modulation coils and the corresponding compensation coils) and is thus known. Since the modulation field is time-dependent it is useful to decompose the local field into selection and modulation components, according to

$$\vec{H}(\vec{r}_s, t) = \vec{H}^{\text{sel}}(\vec{r}_s) + \vec{H}^{\text{mod}}(\vec{r}_s) \cos(2\pi f_{\text{mod}} t). \quad (6)$$

By inserting (6) into (5), and by expanding it in a Fourier series, we get the modulated magnetic moment

$$\vec{\mu}_s(\vec{r}_s, t) = \mu_s \hat{H}(\vec{r}_s, t) \sum_{n \geq 0} m_n(\vec{r}_s) \cos(2\pi n f_{\text{mod}} t), \quad (7)$$

where the coefficients m_n are given by

$$\begin{aligned} m_0(\vec{r}_s) &= \mathcal{L} \left(\frac{|\vec{H}^{\text{sel}}(\vec{r}_s)|}{H_k} \right) \\ m_n(\vec{r}_s) &= \frac{2}{\pi} \int_0^\pi \mathcal{L} \left(\frac{|\vec{H}(\vec{r}_s)|}{H_k} \right) \cos(2\pi n f_{\text{mod}} t) d(2\pi f_{\text{mod}} t) \\ &= \frac{2 |\vec{H}^{\text{mod}}(\vec{r}_s)|}{\pi H_k} \int_{-1}^1 \mathcal{L}' \left(\frac{|\vec{H}^{\text{sel}}(\vec{r}_s) + y \vec{H}^{\text{mod}}(\vec{r}_s)|}{H_k} \right) \\ &\quad \sqrt{1-y^2} U_{n-1}(y) dy, \end{aligned} \quad (8)$$

where $\mathcal{L}'(x) \equiv d\mathcal{L}(x)/dx$ and $U_k(x)$ is the k -th order Chebyshev polynomial of the second kind. We note that for $|\vec{H}^{\text{mod}}(\vec{r}_s)| < H_k$ we have

$$m_1(\vec{r}_s) \approx \frac{|\vec{H}^{\text{mod}}(\vec{r}_s)|}{H_k} \mathcal{L}' \left(\frac{|\vec{H}^{\text{sel}}(\vec{r}_s)|}{H_k} \right) \quad (10)$$

$$m_{n>1}(\vec{r}_s) \approx 0 \quad (11)$$

yielding,

$$\begin{aligned} \vec{\mu}_s(\vec{r}_s, t) &\approx \mu_s \hat{H}(\vec{r}_s, t) \left[\mathcal{L} \left(\frac{|\vec{H}^{\text{sel}}(\vec{r}_s)|}{H_k} \right) + \right. \\ &\quad \left. \frac{|\vec{H}^{\text{mod}}(\vec{r}_s)|}{H_k} \mathcal{L}' \left(\frac{|\vec{H}^{\text{sel}}(\vec{r}_s)|}{H_k} \right) \cos(2\pi f_{\text{mod}} t) \right]. \end{aligned} \quad (12)$$

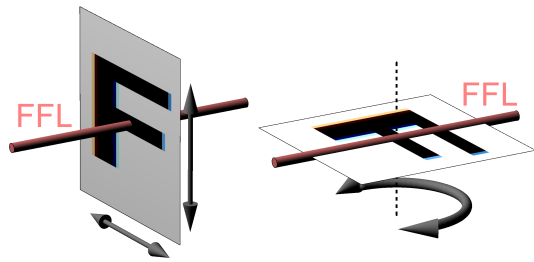


Figure 8: FFP-based (left) and FFL-based (right) 2D scanner sketches. The F symbol represents the MNP distribution in the plane. Pink cylinder represent the FFL. double arrows denote directions of the mechanical motion of the sample.

By inserting Eq. (12) into Eq. (3), and using Eq. (4) yields the detected signal $\delta B_x(\vec{r}_s, t)$. The system's point spread function (PSF) – an example of which is shown in Fig.4 – is then obtained by demodulating the latter at the modulation frequency f_{mod} .

We point out that the signal contains also higher harmonics of f_{mod} since $m_{n>1} \neq 0$ when $|\vec{H}^{\text{mod}}| \geq H_k$ which could lead to a better suppression of the modulation coils' fringe field.

V. Conclusion

In this paper we have proposed a novel design for mechanical MPI scanner operating at low frequency (\leq kHz) based on atomic magnetometry. We have developed a selection coil system which allows to expose the MNP sample to T/m gradient field free line. The atomic magnetometer measures the flux density $\delta B_x \propto M$ produced by the MNP's magnetization M . Modulation coils are deployed to extract the magnetic susceptibility $dM(H)/dH$ proportional to the MNP density on the FFL. Corresponding compensation coils reduce, at the magnetometer location, the fringe field and gradients from the selection

and modulation coils to sufficiently low values that do not compromise the AM's sensitivity. In the near future we plan to realize a mechanical 2D scanner, two possible variants of which are illustrated in Fig.8. The mechanical motion implies a rather slow scan-speed. However, the much lower frequencies than in conventional MPI scanners will make a much broader variety of particles compatible (in particular larger particles) with the MPI method.

Acknowledgements We acknowledge financial support by grant No. 200020 162988 of the Swiss National Science Foundation

References

- [1] B. Gleich and J. Weizenecker. Tomographic imaging using the nonlinear response of magnetic particles. *Nature*, 435:1214–1217, 2005. doi: 10.1038/nature03808.
- [2] T. Knopp and T. M. Buzug. *Magnetic Particle Imaging: An Introduction to Imaging Principles and Scanner Instrumentation*. Springer, Berlin/Heidelberg, 2012.
- [3] P. W. Goodwill, E. U. Saritas, L. R. Croft, T. N. Kim, K. M. Krishnan, D. V. Schaffer, and S. M. Conolly. X-Space MPI: Magnetic Nanoparticles for Safe Medical Imaging. *Adv. Mater.*, 24:3870–3877, 2012. doi: 10.1002/adma.201200221.
- [4] J. Weizenecker, B. Gleich, and J. Borgert. Magnetic particle imaging using a field free line. *J. Phys. D: Appl. Phys.*, 65:105009, 2008. doi: 10.1088/0022-3727/41/10/105009.
- [5] Z. W. Tay, P. W. Goodwill, D. W. Hensley, L. A. Taylor, B. Zheng, and S. M. Conolly. A high-throughput, arbitrary-waveform, mpi spectrometer and relaxometer for comprehensive magnetic particle optimization and characterization. *Sci. Rep.*, 6:34180, 2016.
- [6] E. U. Saritas, P. W. Goodwill, L. R. Croft, J. J. Konkole, K. Lu, B. Zheng, and S. M. Conolly. Magnetic particle imaging (mpi) for nmr and mri researchers. *Journal of Magnetic Resonance*, 229:116–126, 2013.
- [7] S. Colombo, V. Lebedev, Z. Grujic, V. Dolgovskiy, and A. Weis. M(H) dependence and size distribution of spions measured by atomic magnetometry. *International Journal on Magnetic Particle Imaging*, 2(1):1606002, 2016. ISSN 2365-9033.
- [8] S. Colombo, V. Lebedev, Z. Grujic, V. Dolgovskiy, and A. Weis. Mps and acs with an atomic magnetometer. *International Journal on Magnetic Particle Imaging*, 2(1):1604001, 2016.
- [9] D. Budker, D.F. Jackson Kimball (eds.), *Optical Magnetometry* (Cambridge University Press, 2013)
- [10] A. Tonyushkin and M. Prentiss. Straight macroscopic magnetic guide for cold atom interferometer. *J. Appl. Phys.*, 108:094904, 2010.
- [11] A. Tonyushkin. Novel selection coils design for 3D FFL-based MPI. *Proc. 6th Int. Workshop Magn. Particle Imag.*, 2016